

On the precursor times of thermal infrared radiation anomalies before earthquakes in Taiwan

JEEN-HWA WANG (✉ jhwang@earth.sinica.edu.tw)

Institute of Earth Sciences, Academia Sinica

Research Article

Keywords: Earthquake prediction, Earthquake precursor, Thermal Infrared Radiation, Precursor time, Earthquake magnitude

Posted Date: June 14th, 2022

DOI: <https://doi.org/10.21203/rs.3.rs-1736004/v1>

License:  This work is licensed under a Creative Commons Attribution 4.0 International License.

[Read Full License](#)

1 **On the precursor times of thermal infrared**
2 **radiation anomalies before earthquakes in Taiwan**

3
4 JEEN-HWA WANG^{1,2}

5 1. *Institute of Earth Sciences, Academia Sinica, Nangang, Taipei, Taiwan*

6 2. *Department of Earth Sciences, National Central University, Jhongli, Taiwan*

7 E-mail: jhwang@earth.sinica.edu.tw

8 (submitted to Pure and Applied Geophysics on June 08, 2022)

9
10 *Abstract*—Twenty-seven Taiwan’s earthquakes with local magnitudes $M_L=5.6-7.3$
11 and focal depths $d=8.0-215.8$ km were preceded by the thermal infrared radiation
12 (TIR) anomalies. The data set is good for us to explore the precursor times and
13 mechanisms of TIR. Let T_D and T_N be the largest number of days when the anomalies
14 observed in the day-time and the night-time, respectively. The precursor time, T , for
15 an event is the larger value of T_D and T_N . The data points of T versus M_L and those of
16 T_D versus M_L are scattered. Regardless of two data points with abnormally large T_N
17 values, a positive correlation seems able to be recognized from the data points of T_N
18 versus M_L . Among the 27 earthquakes, 8 events were preceded by Rn concentration
19 changes with precursor times $T_{Rn}=7.4-171$ days. For most of the 8 events, T_{Rn} is
20 much longer than either T_D or T_N . Hence, the model of outflow of gases from the
21 depths to the ground surface seems unable to interpret the TIR anomalies. Based on
22 rock mechanics experiments, the temperature rise, ΔT , is generated by frictional
23 heating due to preseismic slip. That the TIR anomalies discontinuously appeared
24 before earthquakes and the occurrence times vary for different events might be due to
25 the generation of frictional heating caused by preseismic slip on a few shallow
26 sub-faults in the source areas before the earthquakes.

27
28 **Keywords:** Earthquake prediction, Earthquake precursor, Thermal Infrared Radiation,
29 Precursor time, Earthquake magnitude

31 *Declarations*

32

33 Funding: the Central Weather Bureau (Grant No.: MOTC-CWB-109-E-02 and
34 MOTC-CWB-110-E-01)

35

36 Conflicts of interest/Competing interests: There are no known competing financial
37 interests or personal relationships that could have appeared to influence the work
38 reported in this paper.

39

40 Availability of data and material: No

41

42 Code availability: No

43

44 Authors' contributions: JHW is responsible for collections of related data, the
45 theoretical studies, numerical computations, and preparing the manuscript.

46

47 Ethics approval: Yes

48

49 Consent to participate: Yes

50

51 Consent for publication: Yes

52

1. Introduction

53

54

55 Since Wang and Zhu (1984) and Gorny *et al.* (1988) made the pioneering work, the
56 anomalies of thermal infrared radiations (TIR) have been long applied for earthquake
57 prediction research (see Ouzounov *et al.* 2018; Tramutoli *et al.* 2018). The TIR or
58 long-wave radiation (LWR), in the spectral range 8–14 μm , that is a short-lived
59 anomaly representing energy emitted from Earth in the form of EM radiation. It
60 passes through the atmosphere and goes into space. The outgoing long-wave
61 radiations (OLR) on the top of atmosphere may be detected by satellites (Ouzounov *et*
62 *al.*, 2018; Tramutolis *et al.*, 2018). The OLR is influenced mainly by several factors,
63 including the near-surface temperature, atmospheric temperatures, humidity of the air,
64 and quantity of clouds. These factors are controlled by the intensity of atmospheric
65 convective activity that depend on latitude and altitude (Ouzounov *et al.*, 2006). Some
66 authors (e.g., Ouzounov *et al.*, 2018; and cited references therein) assumed that the
67 TIR not only reveals stationary (long-lived) thermal anomalies associated with large
68 linear geological structures and fault systems in the crust but also is related to
69 earthquakes. Numerous observations lead to three characteristics of short-lived TIR
70 anomalies: (1) the anomalies commonly appeared 4–14 days before forthcoming
71 earthquakes; (2) the anomalies may lead to a positive deviation of 2–4 $^{\circ}\text{C}$ or more in a
72 region of several to ten thousand square km around the epicenter; and (3) the
73 anomalies decay very fast a few days after the event. Their spatial distributions and
74 temporal variations may be influenced by regional meteorological environments,
75 geological structures, and seismo-tectonics conditions. Numerous studies (e.g.,
76 Ouzounov *et al.*, 2018; and cited references therein) show that thermal anomalous
77 space-time transients may be found in the TIR or LWR before and/or during an
78 earthquake nucleation stage. The main mechanisms proposed to interpret the
79 temperature increases are: (1) the emission of diffused gases, e.g., Rn, CO_2 , etc., thus
80 leading to a local greenhouse effect and/or near-ground air ionization to release heat
81 (Enomoto, 2012; Tramutoli *et al.*, 2013; Ouzounov *et al.*, 2018; and cited references
82 therein); (2) hot water squeezing-out from the deeper parts upwards to the ground
83 surface (Surkov *et al.*, 2006); and (3) positive hole charge (Freund, 2013), thus
84 resulting in thermal infrared emissions and energy flow.

85 In numerous observations (Qiang *et al.*, 1997; Ouzounov and Freund, 2004;

86 Ouzounov *et al.*, 2006, 2007, 2011; 2018; Pulinets and Dunajec, 2007; Pulinets and
87 Ouzounov, 2011; Pulinets *et al.*, 2006, 2018; Tramutoli *et al.*, 2001, 2005, 2013,
88 2018), the time-varying spatial distribution of TIR anomalies seems to be random and
89 varies very much for different earthquakes. Meanwhile, the observed hot spots are
90 very often far away (even several hundred kilometers) from the mainshock epicenters.
91 In addition, the TIR anomalies did not continue with time and appeared only on
92 several days in either day time or night time before forthcoming earthquakes. Of
93 course, for some cases the TIR anomalies appeared only once a few days and then
94 disappeared before forthcoming earthquakes. On the other hand, field surveys,
95 laboratory experiments, and theoretical modelling suggest that the emissions of
96 diffused gases generally continue with time. It is necessary to study the inconsistency.
97 In addition, the authors who studied the TIR anomalies usually do not mention the
98 possible correlation between the precursor time of TIR anomalies and the magnitude
99 of forthcoming earthquake. But, such a correlation is significant for both the basic
100 study of intrinsic properties of TIR and the application of TIR anomalies to hazard
101 reduction (Wang, 2021c).

102 Several authors applied remote-sensing techniques to observe the TIR anomalies
103 before earthquakes in Taiwan (Pulinets and Dunajec, 2007; Pulinets and Ouzounov,
104 2011; Genzano *et al.*, 2015; and Fu *et al.*, 2020). Their studies lead to the precursor
105 times of TIR anomalies before 27 earthquakes. The Rn concentration changes were
106 also observed for some events. These observations give us an opportunity to study the
107 above-mentioned problems.

108 Tsai *et al.* (1977), Tsai (1986), and Wu (1978) proposed that Taiwan is located at an
109 oblique collision zone between the Eurasian plate (EP) and the Philippine Sea plate
110 (PSP). The collision boundary between the two plates is almost along the
111 Longitudinal Valley (LV) which is schematically displayed by a thin line marked with
112 'LV' in Fig. 1. The PSP has been moving northwestward at a speed of ~80 mm/year
113 (Yu *et al.*, 1997) to collide with the EP. In northern Taiwan, the subduction zone of the
114 PSP is beneath the EP. In southern Taiwan, the EP moves from west to east and the
115 subduction zone of the EP is beneath the PSP. Active orogeny due to the collision of
116 these two plates causes strong tectonics and complicated geological features in the
117 region, thus resulting in high and heterogeneous seismicity (Wang 1988, 1998).

118 The time interval between the occurrence of a certain precursor and that of the
119 forthcoming earthquake is called the precursor time, T (Wang *et al.*, 2016; Wang,

120 2021b). In this study, we will first compile the precursor times, T , of TIR/OLR
 121 anomalies before the 27 earthquakes and then explore the possible correlation
 122 between the precursor time and the mainshock magnitude. As suggested by several
 123 authors (e.g., Campbell, 2009; Thomas et al., 2009a,b; Masci, 2010, 2011a,b,c, 2012;
 124 Masci and Di Persio, 2012; Anagnostopoulos, 2021), it is necessary to further study
 125 the reliability and intrinsic significance of observed anomalies based on physical and
 126 chemical mechanisms. In the followings, the earthquake magnitude is the local
 127 magnitude, M_L , determined by the Central Weather Bureau (CWB) (Shin, 1992). The
 128 focal depth of an earthquake is denoted by d (in km) and the epicentral distance from
 129 an event to an observation station is shown by Δ (in km).

130

131

2. Data

132

133 In order to explore the possibility of using OLR as an earthquake precursor,
 134 numerous methods, for example, the robust estimator of OLR anomalies (RETIRA)
 135 by Filizzola *et al.* (2004) and Tramutoli *et al.* (2005), the OLR vorticity value by
 136 Ouzounov *et al.* (2007), the E_{index} method by Pulinets and Ouzounov (2011) and Fu *et al.*
 137 *et al.* (2020), etc., have been used to trace the variation in OLR from the satellite data.
 138 Here, only the E_{index} method is briefly described. The study area is first divided into
 139 $n \times m$ grids, each being denoted by x_{ij} . Let the OLR value at a certain grid, x_{ij} , be O_{ij} .
 140 The yearly average is denoted by $\bar{O}_{ij} = (O_{ij})_{one\ year}$. Hence, the current daily value is
 141 $O^*(x_{ij}; t) = O_{ij} - \sum N_{ij} \bar{O}_{ij}$ where N_{ij} is the number of the surrounding grid points around
 142 the target point. Let $O^*(x_{ij}; t)$ be the average of daily values observed in a time period
 143 of several days, for example 16 days used by Fu *et al.* (2020), excluding the value of
 144 the current day. The residue is represented by $OLR(t)^A = O^*(x_{ij}; t) - \bar{O}^*(x_{ij}; t)$. Fu *et al.*
 145 (2020) defined $E_{Index} = OLR(t)^A / \sigma_{ij}$ where σ_{ij} is the standard deviation. They defined
 146 the standardized anomaly E_{Index} to be the OLR anomaly divided by a standard
 147 deviation. They considered an anomaly (EA) of E_{Index} as the preseismic signal.

148 Genzano *et al.* (2015) observed TIR anomalies before $M > 4$ earthquakes, including
 149 the 1999 $M_L 7.3$ Chi-Chi earthquake, that occurred in Taiwan during 1995–2002.
 150 They observed two significant time sequences of TIR anomalies first appeared 14
 151 days and 12 days, respectively, in the night-time before the Chi-Chi earthquake. The
 152 first sequence appeared in the Taiwan Island and was close to the mainshock

153 epicenter; while the second one occurred in southern China. Clearly, the first
154 sequence may represent the TIR precursor of the earthquake. However, they did not
155 clearly provide the precursor times of TIR anomalies for other $M>4$ events. Hence,
156 only the precursor time of 14 days prior to the 1999 Chi-Chi earthquake is listed in
157 Table 1. In the table, t_D and t_N denote the days when the OLR anomalies were
158 observed in the day-time and night-time, respectively, before related earthquakes.

159 Pulinets and Dunajec (2007) analyzed the transient OLR observed by NASA
160 Aqua/AIRS prior to an $M_L5.6$ (or $M_s5.9$) earthquake (with $d=15.3$ km) that occurred
161 offshore southeast Taiwan on February 19, 2005. They obtained the normalized
162 residual on 4 days in the day-time and on 1, 6, and 9 days in the night-time before the
163 earthquake. Hence, $t_D=4$ days and $t_N=1, 6,$ and $9,$ days for this event are listed in
164 Table 1. Pulinets and Ouzounov (2011) analyzed the transient OLR observed by
165 NASA Aqua/AIRS prior to an $M_L6.0$ (or $M_s6.2$) earthquake (with $d=27.1$ km) that
166 occurred offshore southeast Taiwan on May 19, 2004. They measured the static
167 5-year standard deviation in the time period during May 2003 to December 2007 and
168 the static mean of 18th–20th of five years from 3-day moving mean samples. Finally,
169 they obtained the normalized residual in the time interval of May 18–20, 2004. This
170 led to the appearance of E_{index} anomaly in this time interval. This suggests that the
171 POEA appeared one day before the earthquake. Since they did not mention that the
172 observations were made in the day-time or the night-time. From their plots, it seems
173 that the POEA appeared in the whole day. Hence, $t_D=1$ day and $t_N=1$ day for this
174 earthquake are listed in Table 1.

175 By applying the E_{Index} method, Fu *et al.* (2020) analyzed the satellite data obtained
176 by the National Oceanic and Atmospheric Administration (NOAA), USA for 35
177 $M_L\geq 6$ earthquakes during 2009–2019 in Taiwan. They found that the variation in
178 E_{Index} may be disturbed by the occurrence of a typhoon before an earthquake.
179 Meanwhile, the focal depth, d , of an event is also a significant factor in affecting the
180 variation in E_{Index} . Based on Ustaszewski *et al.* (2012), Fu *et al.* (2020) took $d=70$ km
181 as a criteria to classify the events into two groups: the shallow events with $d\leq 70$ km
182 and the intermediate-depth ones with $d>70$ km. (Note that the location error
183 determined by the CWB is usually higher for offshore events than inland ones.) There
184 were seven intermediate-depth events in their study. Anomalies were observed before
185 three intermediate-depth events with $d=88.0$ km, 73.4 km, and 215.8 km, yet not
186 before four intermediate-depth events with $d=206.2$ km, 268.6 km, 203.7 km, and

187 258.9 km, respectively. Four of the seven intermediate-depth events were located at
188 the northern subduction zone of the PSP and one at the southern subduction zone of
189 the EP. Except for two events with $d=88.0$ km and 73.4 km, these so-called
190 intermediate-depth events are actually very deep. There were 28 shallow events with
191 $d<70$ km. Five shallow events were located at either the Ryukyu Trench or the middle
192 part of the PSP and thus far from Taiwan. Three of the five events were preceded by
193 E_{index} anomalies. In addition to the above-mentioned 12 events, other 23 events were
194 located at the inland area of Taiwan or near the coast in offshore eastern Taiwan. Fu
195 *et al.* (2020) observed consecutive appearances of EAs of LWR about 2–25 days
196 before 24 earthquakes that are 69% of events in their study. They considered this
197 phenomenon as a preseismic OLR E_{Index} anomaly (POEA). The source parameters
198 and observational results of the 24 events are listed in Table 1. From the previous four
199 studies, there are totally 27 events with preseismic TIR anomalies.

200 We re-classify the events into two groups based on the focal depths from an
201 alternative viewpoint. Wang *et al.* (1994) reported that inland earthquakes in Taiwan
202 were located mainly in the depth range 0–12 km. The crust-upper mantle boundary
203 with $v_p=7.5$ km/s in the Taiwan region is mainly in the range 35–45 km as inferred by
204 several authors (e.g. Rau and Wu, 1995; Ma *et al.*, 1996; Kim *et al.*, 2005). Hence, an
205 average depth of 40 km is taken as a boundary to classify the events: a crustal event
206 with $d\leq 40$ km and an upper-mantle or subduction-zone event with $d>40$ km. Hence,
207 the events with $d\leq 40$ km and $d>40$ km are illustrated by open circles and solid circles,
208 respectively, in Fig. 1. From this figure, we can see that 9 events are inland and others
209 offshore. All events with $d>40$ km are offshore and an event, i.e., EQ-13, is far away
210 from Taiwan.

211

212

3. Results

213

214 From Fu *et al.* (2020), we can see that the spatial distribution of POEA is quite
215 random and the POEA discontinuously appeared only on several days in either
216 day-time or night-time before forthcoming earthquakes selected by the authors. The
217 largest values of t_D and t_N for an event are denoted by T_D and T_N , respectively. Table
218 1 shows that except for EQ-02, EQ-04, EQ-07, and EQ-16, the numbers of days with
219 POEA are different between day-time and night-time. Before EQ-01 (i.e., the 1999

220 Chi-Chi earthquake), EQ-15, EQ-20, and EQ-23, the POEA only appeared in the
221 night-time, yet not in the day-time. The POEA did not appeared in the night-time only
222 before EQ-13. Relatively, it seems easier to detect the POEA in the night-time than in
223 the day-time. Figure 2 displays the plot of T_N versus T_D for 22 events having both t_D
224 and t_N . The thin line represents the bisection one.

225 Although the POEA appeared on several days in either day-time or night-time, only
226 the larger value of days for both t_D and t_N before a forthcoming earthquake is taken as
227 the precursor time, T , in this study. Table 1 shows $T=1-25$ days for the 27 events. In
228 order to explore the possible correlation between T and M_L , the plot of T versus M_L is
229 shown in Fig. 3 where the crustal events with $d \leq 40$ km and upper-mantle or
230 subduction-zone events with $d > 40$ km are illustrated by open and solid circles,
231 respectively. In order to further investigate the possible difference on the days of
232 appearance of OLR anomalies between the day-time and the night-time, the plots of
233 T_D versus M_L and T_N versus M_L are shown in Fig. 4a and Fig. 4b, respectively. In Fig.
234 4, the events with $d \leq 40$ km and those with $d > 40$ km are shown by open and solid
235 circles, respectively.

236

237

4. Discussion

238

4.1 Examination of results

240

241 Figure 1 exhibits that the number of offshore events is about two times of that of
242 inland ones. This means that more offshore events than inland ones were proceeded
243 by the POEA. This difference might be explained by two reasons. The first one is that
244 since seismicity in Taiwan is usually higher offshore than inland (Wang, 1998), the
245 number of offshore events with POEA should be larger than that of inland ones. The
246 second one is that on the Taiwan Island, high mountains with thick lands, remarkable
247 topography, and thick vegetation on the land would decrease the surface temperatures
248 that are caused by either emissions of diffused gases from the depths or heat caused
249 by faulting underground. Almost all inland events were located below high mountains
250 which are commonly covered by a large number of plants and thick vegetation. On
251 the other hand, offshore events are covered by sea water. Hence, the TIR anomalies
252 would be lower for inland earthquakes than offshore ones.

253 Fig. 2 shows that except for the two data points with abnormally large T_N values
 254 and one with abnormally large T_D value, the data points are almost around the
 255 bisection line. There 14 events with $T_N \geq T_D$ and 6 events with $T_N < T_D$. This means
 256 that it is easier to detect the OLR in the night-time than in the day-time. From Fig. 1
 257 and Table 1, two events, i.e., EQ-08 and EQ-26, whose largest t_N values are 24 days
 258 for the former and 20 days for the latter were located at eastern Taiwan. EQ-08 with
 259 $d=46.9$ km was offshore and EQ-26 with $d=20.3$ km was inland. The two events are
 260 close to each other with an epicentral distance < 20 km. The difference between the
 261 largest t_N value and the second largest one is 17 days for the former and 18 days for
 262 the latter. From Table 1, we can see that such a difference is much larger than those of
 263 others. In addition, two offshore events, i.e., EQ-6 with $d=43.8$ km and EQ-19 with
 264 $d=38.4$ km, are very close to EQ-8 and not too far from EQ-26. The difference
 265 between the largest t_N value and the second longest one is 1 day for the former and 4
 266 days for the latter. The local tectonic and geological conditions for the four events are
 267 very similar. In addition, EQ-21 (with $d=16.4$ km) that was located at southwestern
 268 Taiwan has the largest t_D value of 25 days. The difference between the largest t_D
 269 value and the second largest one is 16 days which are much larger than those of others.
 270 In addition, two inland events, i.e., EQ-7 with $d=22.6$ km and EQ-10 with $d=26.3$ km,
 271 are very close to EQ-21. The difference between the largest t_N value and the second
 272 largest one is only 1 day for both of them. The local tectonic and geological
 273 conditions for the three events are very similar. It is very interesting to ask why the
 274 largest t_N values of POEA for EQ-08 and EQ-26 and the largest t_D values for EQ-21
 275 are much bigger than those for others. As listed in Table 1, the largest t_N value for
 276 EQ-01, i.e., the 1999 $M_L 7.3$ Chi-Chi earthquake, is only 14 days. For world-wide
 277 earthquakes, the POEA commonly appeared about 4–14 days before forthcoming
 278 earthquakes (Ouzounov *et al.*, 2018; and cited references therein). For example, the
 279 POES appeared only about five days before the $M_s 9$ great Tohoku, Japan, earthquake
 280 of March 11, 2011 (Ouzounov *et al.*, 2011). Hence, the precursor times of EQ-08,
 281 EQ-21, and Eq-26 seem too long. The reasons to cause such very long precursor times
 282 are unknown. I assume that such a particularly early POEA was not caused by
 283 preseismic slip and thus the three values might not be the real precursor times.

284 Although the data points are quite scattered in Fig. 3, T still slightly increases with
 285 M_L when three data points with abnormally high T as mentioned above are removed.
 286 Fig. 4a for T_D versus M_L displays that the data points are quite scattered. Although T_D

287 slightly increases with M_L , not any correlation between T_D and M_L can be recognized.
288 The data points in Fig. 4b for T_N versus M_L are also scattered. Nevertheless, the
289 degree of scattering of data points seems lower in Fig. 4b than in Fig. 4a. This
290 suggests that it is better to observe the preseismic POEA in the night-time than in the
291 day-time. However, a high degree of scattering of data points for both T_D and T_N
292 might downgrade the feasibility of using the preseismic POEA for earthquake
293 prediction.

294

295 4.2 Models of heat due to diffused gases and hot water

296

297 As mentioned above, several mechanisms have been proposed to interpret the
298 temperature increases on the Earth's ground surface for generating TIR. Freund (2013)
299 assumed that the upward outflow of stress-induced positive-hole charges from the
300 source area to the ground surface results in TIR and energy flow. However, Putinets *et*
301 *al.* (2018) strongly claimed that the model proposed by Freund (2013) is wrong
302 because not any upward outflow of positive-hole charges from the ground has been
303 observed. Hence, this mechanism will not be further discussed here.

304 The emissions of diffused gases, e.g., Rn, CO₂, etc., from the deeper crust to the
305 ground surface lead to a local greenhouse effect or near-ground air ionization that
306 releases heat (Enomoto, 2012; Tramutoli *et al.*, 2013; Ouzounov *et al.*, 2018). ²²²Rn
307 first decays, with a half time of 3.8 days, to ²¹⁸Po and then again decays, with a half
308 time of 3.85 minutes, to ²¹⁴Pb (cf. Scholten *et al.*, 2013). During the two decaying
309 processes, there are α -particle (i.e., ⁴He) emissions with energy release of 5.49 MeV
310 in the first step and 6 MeV in the second one. This is a direct way to release heat and
311 thus increase the temperature on the ground surface. It is assumed that Rn
312 concentration changes may be influenced by different effects caused by forthcoming
313 earthquakes. From the Rn concentrations measured at a station near a volcanic area in
314 northern Taiwan, Liu *et al.* (1984) found that a very high Rn concentration appeared
315 in the gases (mainly CO₂) with hot water that discharged from the well. They
316 assumed that hot water is very susceptible to Rn loss. They also claimed that the
317 spatial distribution of events which occurred after the appearance of Rn concentration
318 anomalies is not uniform and skewed in certain directions from the Rn monitoring
319 stations. This seems to suggest that Rn concentration changes are sensitive to

320 earthquakes that occurred in some directions and insensitive to those in others. The
321 surface temperature will be increased due to energy release caused by emissions of Rn
322 and CO₂ for some earthquakes, yet not for others. Kuo *et al.* (2010) observed the Rn
323 concentrations at the Antung station in eastern Taiwan decreased from background
324 levels to the minima before three local earthquakes. They applied the radon-
325 volatilization model and the rock-dilatancy model to interpret the decrease in Rn
326 concentrations. A decrease in Rn concentrations will reduce the energy release and
327 thus cannot enhance the temperature on the ground surface. This will not lead to the
328 POEA before some earthquakes.

329 For the emissions of CO₂ and some gases, Tramutoli *et al.* (2013) assumed that the
330 fluids in the foot walls of a fault, for example the fault related to the M_w 6.3 L'Aquila,
331 Italy, earthquake of April 6, 2009, flowed upwards to the hanging walls in a time
332 interval before the forthcoming earthquake and thus brought some active gases (e.g.,
333 CO₂ and CH₄) to reach the ground surface. Those gases would spread in the lower
334 part of the atmosphere and then produce the local greenhouse effect that is responsible
335 for the TIR anomalies. They also considered that such CO₂-rich sources might be a
336 little far away (for instance several ten kilometers) from the epicentral area. Hence,
337 the TIR/OLR anomalies might appear somewhat far away from the forthcoming
338 earthquake. However, there is a question about their model. The fluids flowed from
339 the foot walls below a fault to the hanging walls above the fault. I wonder if the
340 upward fluids can flow to gases-rich sources that a little far away from the fault and
341 then bring the gases to reach the ground surface or not because the rocks outside a
342 fault zone are usually solid and compact. Enomoto (2012) assumed that a coupled
343 interaction between earthquake nucleation and deep gases in the source area leads to
344 outflow of gases. Surkov *et al.* (2006) proposed a theoretical model for temperature
345 increases on the ground surface near the faults. They assumed that a tectonic stress in
346 the source area results in water squeezing-out from the deeper parts upwards to the
347 ground surface. A convection mechanism of warming rocks caused by upward hot
348 groundwater may be responsible for stable temperature anomalies arising near the
349 fault. This mechanism will be the main one to make the gases discharge from the
350 deeper parts of crust upwards to the ground surface as mentioned in the last
351 mechanism. From the two models, the TIR/OLR anomalies should appear near or not
352 too far away from the forthcoming earthquake.

353 It is interesting and significant to ask if the earthquakes having preseismic

354 TIR/OLR anomalies in Table 1 were also preceded by Rn concentration changes or
355 not. From scientific literature, we found that Rn concentration changes were observed
356 before eight events that are 29.6% of the 27 earthquakes listed in Table 1. The T_D
357 values, T_N values, and the precursor times of Rn concentration changes (denoted by
358 T_{Rn}) with related references are listed in Table 2. For EQ-02, it seems that the
359 TIR/OLR anomalies might be caused by the mechanism of energy release due to
360 α -particles that were produced from the decay process of ^{222}Rn because $T_{Rn}=7.4$ days
361 from Yang *et al.* (2005) is larger than $T_D=1$ day and $T_N=1$ day. For EQ-19, $T_{Rn}=9$
362 days from Fu *et al.* (2019) is smaller than $T_D=12$ days and equal to $T_N=9$ days. This
363 event is on the margin of the application of energy release for TIR/OLR anomalies
364 due to α -particles. For the rest six events, T_{Rn} is much larger than either T_D or T_N .
365 Hence, the possibility to produce the TIR/OLR anomalies by energy release due to
366 α -particles is low because the half-time of the decay process from ^{222}Rn to ^{214}Pb is
367 only about 3.8 days. Meanwhile, for EQ-07, EQ-12, and EQ-15, the Rn
368 concentrations decreased from the respective normal values to the minima before the
369 earthquakes happened (Kuo *et al.*, 2018, 2019). Hence, it is impossible to apply the
370 mechanism of emissions of gases to interpret the TIR/OLR anomalies. For EQ-21,
371 T_{Rn} is 54 days from the depths measured by Kuo *et al.* (2018) at a station with $\Delta=45$
372 km and 14 days observed by Fu *et al.* (2017a) at five stations with with $\Delta=31-212$ km.
373 The mechanism fails for the former but works well for the latter. Essentially, the six
374 stations that are surrounding EQ-21 and in southwest Taiwan have similar tectonic
375 and geological conditions. It is hard to understand why there is a big difference
376 between Kuo *et al.* (2018) and Fu *et al.* (2017a). The Rn concentration changes before
377 EQ-7 were detected by Kuo *et al.* (2018, 2019) at the same station, yet not by Fu *et al.*
378 (2017a). The Rn concentration changes before EQ-10 that were close to EQ-07 and
379 EQ-21 were not detected by the two groups. In addition, a few events without
380 preseismic TIR/OLR anomalies in Fu *et al.* (2020) were preceded by Rn
381 concentration changes. From the previous discussion, it seems that the mechanism of
382 energy release due to α -particles that were produced from the decay process of ^{222}Rn
383 to ^{214}Pb cannot completely and reliably interpret the preseismic TIR/OLR anomalies.

384 Hot springs are abundant and active in Taiwan (Lee and Cheng, 1986) and volcanic
385 activities are also remarkable in northern Taiwan as well as several offshore areas
386 (Lin, 2016). Hot springs and volcanic activities can produce a time-varying

387 non-uniform spatial distribution of heat in the Taiwan region (Barr and Dahlen, 1989;
388 Wang *et al.*, 1994; Lin, 2000; Ma and Song, 2004; Wu *et al.*, 2013). Chan and Chang
389 (2018) and Chan *et al.* (2018, 2020) also observed the effects of activities of hot
390 springs and volcanoes on the TIR in Taiwan. Chan and Chang (2018) estimated the
391 surface temperatures on the Tatung Volcano Group (TVG) in Northern Taiwan from
392 TIR during 2002–2018. In the time period of their observations, two $M_L > 4$
393 earthquakes occurred below the TVG. However, we cannot see anomalies before the
394 two events from the temporal variations in surface temperatures, i.e., Fig. 5 in Chan
395 and Chang (2018). A possible reason is that the surface temperatures caused by the
396 hot springs and volcanoes are much higher than those produced by the two events.
397 This confirms the importance of the effects of activities of hot springs and volcanoes
398 on the TIR/OLR. Tronin *et al.* (2002) stressed that volcanoes result in abnormally
399 high values of convective heat flow. The theory proposed by Surkov *et al.* (2006) also
400 suggests that hot water which came from the depths of hot springs or volcanoes flows
401 upwards to the ground surface and thus may be considered as a source to enhance the
402 surface temperature for generating TIR/OLR. This will influence the time-varying
403 spatial distribution of TIR/OLR anomalies. In principle, the data processing on the
404 estimates of E_{Index} anomalies must eliminate the long-term effect due to hot water
405 from hot springs and volcanoes. But, the four groups of authors who provided the 27
406 events in Table 1 did not clearly mention this point. Hence, we do not exactly know if
407 such an effect has been completely eliminated or not.

408

409 *4.3 Model of heat caused by preseismic slip*

410

411 In addition to the above-mentioned three mechanisms, we here consider a different
412 mechanism that the TIR/OLR may be caused by frictional heat which is generated by
413 preseismic slip on the fault plane related to a forthcoming earthquake. During faulting,
414 radiation energy, fracture energy, and frictional energy can be produced on the fault
415 plane and the frictional energy can be transferred to heat (Wang, 2006; and cited
416 references therein). Since the detailed description of heat generation on a fault plane
417 can see Wang (2006), only a simple explanation is given below. Due to preseismic
418 slip, the frictional energy, E_f , produced by a dynamic friction stress, σ_d , on the fault
419 plane is $E_f = \sigma_d A u$ where A and u are, respectively, the slipped area and the preseismic

420 slip. The heat strength is $Q=E_f/C\rho A$ where C and ρ are, respectively, the specific heat
421 and density of fault-zone rocks and they usually do not change too much in different
422 fault-zone rocks. In general, C is 10^3 J/kg-°C and ρ is 2.6×10^3 kg/m³. The heat
423 strength may leads to a temperature rise in the fault zone with a thickness of h :

424

$$425 \quad \Delta T=Q/h=\sigma_d u/C\rho h. \quad (1)$$

426

427 Equation (1) shows an increase of ΔT with $\sigma_d u$ which is time-increasing frictional
428 energy per unit area. On the other hand, ΔT decreases with increasing h . The wear
429 processes occurring during brittle faulting could widen h (Hull, 1988; Marrett and
430 Allmendinger, 1990). The degree of wear processes is time-increasing. Hence, h can
431 influence not only the long-term earthquake recurrence (Wang, 2018) but also the
432 generation of frictional heat. A young fault with thin h is more capable of generating
433 high frictional heat than a mature one with thick h . This suggests that the POEA
434 anomalies should appear earlier before a young fault than a mature one when they had
435 the same preseismic slip. Meanwhile, this may be one of the reasons why we cannot
436 observe TIR/OLR anomalies before some earthquakes that might rupture along
437 mature faults.

438 The detailed description about temporal variations in preseismic stress and slip can
439 see Wang (2021a). Only a simple explanation is given below. The stress σ usually
440 varies with time (Atkinson, 1984; Rudnicki, 1988; Main and Meredith, 1989) as
441 schematically displayed in Fig. 5a. There are three stages, i.e., Stages 1–3, before the
442 earthquake occurrence at $t=t_r$ and two stages, i.e., Stages 4 and 5, during and after the
443 event. In general, the time period is the longest in Stage 1 from t_o to t_y and the shortest
444 in Stage 4. Since only the precursor is taken into account in this study, Stages 4 and 5
445 will not be further explained. In Stage 1 elastic buildup of strain energy starts at t_o and
446 stops at t_y when the elastic (linear) loading transfers to plastic (nonlinear) loading.
447 The changing point from elastic loading to plastic loading is called the yielding point.
448 Stage 2 (occurring from t_y to t_m when the loading stress reaches its peak) displays
449 plastic strain hardening due to dilatancy because of crack coalescence and fluid
450 transport in the fault zone. In Stage 3 ($t=t_m$ to t_r) the loading stress decreases and
451 demonstrates precursory stress drop or strain softening. The time period of this stage
452 is several months. Stage 3 has three steps: (3a) for micro-crack linkage, (3b) for pore

453 fluid diffusion, and (3c) for quasi-static slip on the fault between asperities.

454 An earthquake occurs after failure of asperities on a fault (Kanamori and Stewart,
455 1978; Kanamori and Heaton, 2000). The stresses concentration appears on the edges
456 of crack tip. Irwin (1958) suggested the stress intensity factor, K , to describe stress
457 concentration. It is defined as (Lawn and Wilshaw, 1975; Scholz, 1990)

458

$$459 \quad K=Y\sigma u^{1/2} \quad (2)$$

460

461 where Y is a geometrical factor and u is the length (equal to the original length plus
462 expansion length) of a crack or a fault responsible for stress concentration. The K also
463 represents the resistance to fracture, and its critical value (denoted by K_c) rather than
464 that of σ controls the rupture time. The temporal variation in K is displayed in Fig. 5b.
465 Experimental and field data reveal that subcritical crack extension with $K < K_c$ can
466 happen due to chemical stress corrosion (Meredith and Atkinson, 1983; Atkinson,
467 1984). The main factor to produce chemical stress corrosion is water that exists
468 widely in fault-zone rocks (Sibson, 1977). The K increases with time and reaches its
469 local maximum at time t_m , then decreases with increasing time, and increases again to
470 K_c within Step 3c. In Step 3c, σ decreases with increasing time and K increases with
471 time due to a remarkable increase in u that compensates a reduction in σ .

472 Experimental results indicate that the velocity of crack extension, $u_t (=du/dt)$, may
473 be described by:

474

$$475 \quad u_t = \dot{A} K^n \quad (3)$$

476

477 where \dot{A} is a constant and n is the stress corrosion or subcritical crack growth index.
478 The two parameters are influenced by temperature, grain size of rocks, and pore fluid
479 pressure. The value of n is commonly between 20 and 60 for earth's materials
480 (Meredith and Atkinson, 1983; Atkinson and Meredith, 1987). Generally, u_t increases
481 with temperature and decreases with increasing grain size of rocks.

482 Define $\delta\sigma = \sigma_m - \sigma_o$ to be an increase in stress from σ_o to σ_m . Assuming that $\delta\sigma$ is
483 much smaller than σ_o and based on Equations (2) and (3), Das and Scholz (1981) and
484 Main (1988) got an approximated solution:

485

486
$$u/u_o=(1-t/t_r)^{2/(2-n)} \quad (t \leq t_r) \quad (4)$$

487

488 where $t_r=2(u_o/u_{to})/(n-2)(1+n\delta\sigma/2\sigma_o)$ is the occurrence time of the forthcoming
 489 earthquake; and u_o and u_{to} are, respectively, the initial crack length and initial crack
 490 velocity. In Equation (4), $t=t_r$ is the singular point of the equation when the
 491 earthquake happens. Equation (4) is simply displayed by a thin solid line in Fig. 5b. A
 492 detailed description about dependence of u on n is given in Fig. 6. The u increases
 493 with decreasing n , thus indicating that the fault-zone rocks with small n is more
 494 capable of producing a large event than those with large n . Meanwhile, u increases
 495 very slowly with time before Step 3c and then increases abruptly with time within this
 496 sub-step until failure of an event.

497 Substitution of Equation (4) into Equation (1) lead to

498

499
$$\Delta T=(\sigma_d u_o/C\rho h)(1-t/t_r)^{2/(2-n)} \quad (t \leq t_r). \quad (5)$$

500

501 The temperature rise increases with dynamic stress, initial slip, and time, but
 502 decreases with increasing thickness of fault-zone rocks because specific heat and
 503 density do not change too much as mentioned above. This temperature rise will
 504 diffuse outwards and partly goes upwards to the ground surface, thus resulting in the
 505 TIR. Fig. 7 displays the temporal variations in ΔT for different values of n when other
 506 six physical parameters are fixed. Regardless of the scaled factor, the temporal
 507 variations of ΔT are similar with those of u/u_o . In Fig. 7, a thin horizontal line
 508 represents the critical temperature rise that may leads to high surface temperature for
 509 generating the TIR. The intersection point of the line with each curve denotes the time
 510 when the TIR may occur. Figure 7 shows that the TIR will appear earlier for a larger
 511 event with small n than a small one with large n . From Figs. 5 and 7, ΔT directly
 512 increases with time and its value becomes large in Step 3c which is usually several to
 513 ten days before a forthcoming earthquake (e.g., Wang, 2021b). In case that this
 514 mechanism is the acceptable one of making the temperature rise on the ground surface,
 515 the time interval of appearance of high surface temperature may happen in the time
 516 interval 2–14 days, with the longest one for EQ-01, i.e., the 1999 $M_L7.3$ Chi-Chi
 517 earthquake. Since the Chi-Chi earthquake is the largest one in Table 1, the precursor
 518 times of other events should be shorter than 14 days. Therefore, the observations of

519 $T_D=25$ days and $T_N=20$ and 24 days should be questionable.

520 There is a question: How thick is the layer within which the temperature rise is
521 produced from preseismic slip? We should concern the underground geological
522 structures. Fig. 8 shows the structure and stress system of the upper crust. The right
523 inclined line represents the depth-increasing lithostatic stress and the left line displays
524 the depth-increasing hydrostatic pressure. Sibson (1992) proposed that in the crust,
525 the transition from hydrostatic regime to a suprahydrostatic one may occur across a
526 permeability barrier or through a progressive transition with depth to the lower
527 permeability crust. Based on the depth distribution of permeability, Zencher *et al.*
528 (2006) called the barrier the transition layer whose topmost depth is deeper than 2.5
529 km for the San Andreas fault, USA (Yerkes et al., 1985). However, the depth range of
530 permeability barrier in Taiwan cannot be estimated because of a lack of depth
531 distribution of permeability. Meanwhile, the topography of the Taiwan region varies
532 very much, from 0 to ~4000 m. This makes the topmost depth of the permeability
533 barrier be remarkably non-uniform. We may try an indirect approach to estimate the
534 possible topmost depth of the permeability barrier in Taiwan. Unsworth *et al.* (1997)
535 conducted the magnetotelluric (MT) surveys across the San Andreas fault at Parkfield,
536 California, USA. Their resistivity structure inferred from MT data reveal that the fault
537 zone is characterized by a low-electric-resistivity (0.26 Ω -m) wedge that is almost
538 shallower than 2 km. When the depth is deeper than 2 km, the electric resistivity
539 remarkably increases. Of course, the depth distributions of electric resistivity are not
540 similar in the two sides of the San Andreas fault. Chen and Chen (2000) conducted
541 the MT soundings along eight profiles across the Sanyi-Puli seismic zone in
542 northwestern Taiwan. The events EQ-01, EQ-05, EQ-12, and EQ-15 occurred almost
543 in the area. They found low electric resistivity in the topmost layer of ~2 km below
544 the sea level and then the electric resistivity increases with depth. This implicates that
545 the thickness of hydrostatic regime is ~2 km in the area. The real thickness of
546 hydrostatic regime in Taiwan should be larger than 2 km when the mountains are
547 taken into account. For simplicity, we consider the average thickness of hydrostatic
548 regime in Taiwan to be 2 km. According to Fig. 8, the above-mentioned question may
549 be considered as: How deep is H within which the temperature rise may be high
550 enough for producing TIR anomalies? This problem will be discussed below.

551 Hot water may come from the deep crust. Surkov *et al.* (2006) assumed that such

552 hot water is capable of diffusing upwards through the structures of channels that are
553 formed by fractures and cracks in the upper layers of the crust having the thickness of
554 about several kilometers. From the model by Enomoto (2012), the up-going hot gases
555 come from the source area and thus the depths of producing temperature rise are
556 almost the focal depths of forthcoming earthquakes. For the model proposed by
557 Tramutoli *et al.* (2013), the depths of sources of gases should be shallower than the
558 focal depths of forthcoming earthquakes, even though the up-going water came from
559 the foot walls of related faults. In order to make the fluids and gases easily flow
560 upwards, the sources of gases should be in the layers above the permeability barrier or
561 transition zone. After the temperature rise has been produced, the temperature may
562 conduct and/or diffuse outwards (e.g., Turcotte and Schbert, 1982). The temperature
563 will decrease with increasing distance from the source and decays with increasing
564 time. In case that the heat should conduct or diffuse a long distance from its source to
565 the ground surface, it will not easy to result in a high enough surface temperature rise
566 for generating the TIR. Hence, the source of heat generation cannot be too deep and
567 should be above the permeability barrier or transition zone.

568 As mentioned above, the TIR leads to a temperature rise of 2–4 °C or more in a
569 region of several to tens of thousands square km around the epicenter. Hence, ΔT
570 should be higher than 4 °C in the heat sources at depths, because ΔT will decrease
571 when the heat transfers from the depths to the ground surface. From Equation (1) with
572 $C=10^3 \text{ J/kg-}^\circ\text{C}$ and $\rho=2.6\times 10^3 \text{ kg/m}^3$, $\Delta T>4 \text{ }^\circ\text{C}$ leads to $\sigma_d(u/h)>4C\rho=1.04\times 10^7 \text{ J/m}^2$,
573 where u/h is the strain in the fault zone along the direction of thickness. In order to
574 generate the electromagnetic precursors, Wang (2021a) assumed that the stress-
575 induced electric field produced by preseismic slip occurs in the uppermost several
576 hundred meters of the crust. He estimated the average normal stresses, σ_n , in the
577 hydrostatic regime (see Fig. 8) for three faulting types. The upper-bound value is 30
578 MPa when H is equal to the thickness of hydrostatic regime ($\approx 2 \text{ km}$). In the
579 uppermost layer with a thickness of 2 km, friction behaves as velocity-strengthening
580 (see Marone, 1998). This means that dynamic friction, σ_d , is higher than static friction
581 $\sigma_s=f_s\sigma_n$ where f_s is the static friction coefficient. This should also be held for the
582 preseismic slip even though the velocity is low. From Equation (4), the preseismic
583 velocity, u_t , is

584

$$585 \quad u_t = u_o [2/(n-2)t_r] (1-t/t_r)^{n/(n-2)} \quad (t \leq t_r). \quad (6)$$

586

587 Equation (6) exhibits that u_t increases with time and is low before Step 3c because u_o
 588 is usually very small. Of course, u_t becomes high in Step 3c. Although u_t is low
 589 before Step 3c, the effect of velocity-strengthening friction still results in $\sigma_d > \sigma_s = f_s \sigma_n$.
 590 Since f_s is usually in the range 0.60–0.75 (e.g., Marone, 1998), σ_d must be higher
 591 than $(0.60-0.75)\sigma_n$ or 18.0–22.5 MPa for the upper bound $\sigma_n = 30$ MPa. It seems
 592 acceptable to take 30 MPa as the upper bound of σ_d in the hydrostatic regime. This
 593 gives $u/h > 0.347$. For $M > 6$ earthquakes, h ranges from 1 m to 50 m from borehole
 594 drilling (e.g., Wang, 2021a). For such earthquakes, we have $u > 0.347$ m for $h = 1$ m and
 595 $u > 17.333$ m for $h = 50$ m. Since the preseismic slip cannot be very large, it should
 596 occur along the sub-faults, with small h , rather than the main fault along which the
 597 forthcoming earthquake will happen. Such sub-faults should be related to the main
 598 fault.

599 The pre-seismic slip may be due to four seismic phenomena, i.e., foreshocks, the
 600 slow earthquakes (including deep episodic tremor, low-frequency earthquakes, very-
 601 low-frequency earthquakes, slow slip events and silent earthquakes) (e.g., Kano et al.,
 602 2018), the nucleation phases (e.g., Wang, 2017), and micro-fracturing (Molchanov
 603 and Hayakawa, 1995). Wang (2021a) assumed that preseismic slip is likely produced
 604 by nucleation phases and micro-fractures. The amplitude of nucleation phases is
 605 commonly very short and the phase usually appeared only several ten seconds before
 606 an earthquake. This suggests that the nucleation phases cannot produce the TIR.
 607 Hence, micro-fracturing may play the main role on the generation of TIR anomalies.
 608 The dimension of micro-fractures ranges 10^{-4} – 10^{-1} m (Molchanov and Hayakawa,
 609 1995). Hence, the TIR anomalies must be produced in sub-faults with a thickness
 610 being shorter than 1 m. When such sub-faults are directly linked to the main one of
 611 the forthcoming earthquake, the TIR anomalies may appear near the mainshock
 612 epicenter. When such sub-faults are not directly linked to the main one, the TIR
 613 anomalies could appear somewhat far away from the mainshock epicenter. Of course,
 614 when the physical conditions on the sub-faults are not suitable for the formation of
 615 preseismic slip, the TIR anomalies will not be generated before an earthquake. This
 616 interprets why some earthquakes were not preceded by the TIR/OLR anomalies.

617 As listed in Table 1, numerous observations (e.g., Ouzounov *et al.*, 2018; Fu *et al.*,

618 2020) show that the POEA did not continue with time and appeared only on a few
619 days in either day-time or night-time before forthcoming earthquakes. Meanwhile, the
620 number of days in which the POEA were detected varies for different events. From
621 field surveys and theoretical modelling as mentioned above, the emission of diffused
622 gases generally continue with time. The Rn concentrations usually either increase or
623 decrease with time until the occurrence of forthcoming events (Wakita *et al.*, 1980,
624 1986; Liu *et al.*, 1984; Kuo *et al.*, 2010, 2018, 2019; Fu *et al.*, 2017a,b; Fu and Lee,
625 2018). Of course, some fluctuations may appear on the temporal variations because of
626 increases or decreases in Rn concentrations caused by background seismicity,
627 foreshocks, and other geological reasons. Based on eq. (4), the preseismic slip
628 increased with time before a forthcoming earthquake. When the frictional heat is high
629 enough due to the appearance of long enough preseismic slip, the TIR/OLR may
630 occur and should continuously increase with time because preseismic slip increases
631 with time. This makes the POEA continuously increase with time. Clearly, there is
632 inconsistency between observations of POEA and theoretical results. This is a sort of
633 evidence to suggest that the frictional heat is not generated on the main fault where
634 the forthcoming earthquake will happen because the preseismic slip should occur
635 continuously in a very long time period before the event. On the other hand, the
636 abnormal temperature rise that produces the POEA is generated by frictional heating
637 due to the preseismic slip on the sub-faults in the shallow part of the source area of a
638 forthcoming earthquake as suggested previously. Those sub-faults did not slip
639 simultaneously because their physical conditions are not the same. The preseismic slip
640 on a sub-fault started to move and then stopped in a short time interval. The number
641 of such sub-faults may be distinct for different forthcoming earthquakes because of
642 different seismogenic conditions. This leads to the observations that the POEA
643 appeared only on a few days in either the day-time or the night-time before
644 forthcoming earthquakes.

645

646

6. Conclusions

647

648 From Pulinets and Dunajek (2007), Pulinets and Ouzounov (2011), Genzano *et al.*
649 (2015), and Fu *et al.* (2020), the TIR/OLR anomalies preceded 27 earthquakes
650 with $M_L=5.6-7.3$ and $d=8.0-215.8$ km in Taiwan. Three types of precursor times are

651 in use: T_D is the largest number of days when the anomalies observed in the day-time;
652 T_N is the largest number of days when the anomalies observed in the night-time; and T
653 that is the larger value of T_D and T_N is taken as the precursor time for an event. The
654 T_D value of an event and the T_N values of two events are abnormally large and
655 questionable.

656 The data points of the plot of T versus M_L is scattered. Nevertheless, the correlation
657 between T and M_L is positive when the data points with abnormally large T values are
658 excluded. The data points of the plot of T_D versus M_L are scattered. Regardless of two
659 data points with abnormally large T_N values, a positive correlation can be recognized
660 from the data points of T_N versus M_L . Hence, it seems better to observe the TIR/OLR
661 anomalies in the night-time than in the day-time.

662 Among the 27 earthquakes, 8 events were preceded by Rn concentration changes
663 with precursor times, T_{Rn} , ranging from 7.4 to 171 days. For most of the 8 events, T_{Rn}
664 is much longer than either T_N or T_D . Meanwhile, for several events Rn concentrations
665 decreased from the background levels to the minima. Hence, the mechanism of energy
666 release due to α -particles that were produced from the decay process of ^{222}Rn to ^{214}Pb
667 cannot completely and reliably interpret the preseismic TIR/OLR anomalies.

668 Based on rock mechanics experiments, there is a theory about the production of
669 temperature rise, ΔT , from frictional heating due to preseismic slip. The thickness of a
670 fault zone is an important factor in influencing the temperature rise. From the theory
671 and the underground crustal structure, the preseismic slip should occur in the topmost
672 layer, with a thickness of 2 km, of the crust. In principle, ΔT continuously increases
673 with time. On the other hand, the observations show that the TIR/OLR anomalies
674 appeared discontinuously before forthcoming earthquakes and the occurrence times
675 vary for different earthquakes. There is inconsistency between the results of models
676 and the observations. A possible mechanism is that the temperature rise caused by
677 frictional heating due to preseismic slip which happened in the different short time
678 intervals on a few shallow sub-faults in the source areas of forthcoming earthquakes.

679

680

Acknowledgments

681

682 This study was financially supported by the Central Weather Bureau (Grand No.:
683 MOTC-CWB-110-E-01) and Institute of Earth Sciences, Academia Sinica, TAIWAN.

684

685

686

REFERENCES

687 Anagnostopoulos, G. (2021). On the origin of ULF magnetic waves before the
688 Taiwan Chi-Chi 1999 Earthquake. *Frontiers in Earth Sciences*, 9, 730162. doi:
689 10.3389/feart.2021. 730162

690 Atkinson, R.K. (1984). Subcritical crack growth in geological materials. *Journal of*
691 *Geophysical Research*, 89, 4077-4114.

692 Atkinson, B.K., & Meredith, P.G. (1987). Experimental fracture mechanics data for
693 rocks and minerals. In: Atkinson, B.K. (Ed.), *Fracture Mechanics of Rock*,
694 Academic Press, London, UK, pp477-525.

695 Barr, T.D., & Dahlen, F.A. (1989). Mountain building 2. Thermal heat budget.
696 *Journal of Geophysical Research*, 94, 3923-3947.

697 Campbell, W.H. (2009). Natural magnetic disturbance fields, not precursors,
698 preceding the Loma Prieta earthquake. *Journal of Geophysical Research*, 114,
699 A05307, doi:10.1029/2008JA013932.

700 Chan, H.P., & Chang, C.P. (2018). Exploring and monitoring geothermal and
701 volcanic activity using satellite thermal infrared data in TVG, Taiwan.
702 *Terrestrial, Atmospheric and Oceanic Sciences*, 29, 387-404, doi:10.3319/TAO.
703 2018.01.22.01.

704 Chan, H.P., Chang, C.P., & Dao, P.D. (2018). Geothermal anomaly mapping using
705 landsat ETM+ data in Ilan plain, Northeastern Taiwan. *Pure and Applied*
706 *Geophysics*, 175, 303-323, doi:10.1007/s00024-017-1690-z.

707 Chan H.P., Chang, C.P., Lin, T.H., Blackett, M., Kuo-Chen, H., & Lin, A.T.S. (2020).
708 The potential of satellite remote sensing for monitoring the onset of volcanic
709 activity on Taipei's doorstep. *International Journal of Remote Sensing*, 41,
710 1372-1388, doi:10.1080/ 01431161.2019.1667549.

711 Chen, C.c., & Chen, C.s. (2000). Preliminary report on the Sanyi-Puli seismic zone
712 conductivity anomaly and its correlation with velocity structure and seismicity in
713 the Northwestern Taiwan. *Earth, Planets and Space*, 52, 377-381.

714 Das, S., & Scholz, C.H. (1981). Theory of time-dependent rupture in the earth.
715 *Journal of Geophysical Research* 86, 6039-6051.

- 716 Enomoto, Y. (2012). Coupled interaction of earthquake nucleation with deep Earth
717 gases: a possible mechanism for seismo-electromagnetic phenomena.
718 *Geophysical Journal International*, 191, 1210-1214.
- 719 Filizzola, C., Pergola, N., Pietrapertosa, C., & Tramutoli, V. (2004). Robust satellite
720 techniques for seismically active areas monitoring: a sensitivity analysis on
721 September 7th 1999 Athens's earthquake. *Physics and Chemistry of the Earth*, 29,
722 517-527.
- 723 Freund, F.T. (2013). Earthquake forewarning – a multidisciplinary challenge from the
724 ground up to space. *Acta Geophysica*, 61(4), 775-807.
- 725 Fu, C.C., & Lee, L.C. (2018). Continuous monitoring of fluid and gas
726 geochemistry for seismic study in Taiwan. In: Ouzounov, D., Pulinets, S.,
727 Hattori, K., Taylor, P. (Eds.), *Pre-Earthquake Processes: A Multidisciplinary*
728 *Approach to Earthquake Prediction Studies*, AGU Geophys. Monog. Series
729 234, 199-218.
- 730 Fu, C.C., Lee, L.C., Ouzounov, D., & Jan, J.C. (2020). Earth's outgoing longwave
731 radiation variability prior to $M \geq 6.0$ earthquakes in the Taiwan area during
732 2009–2019. *Frontier of Earth Sciences*, 8, 364, doi:10.3389/feart.2020.00364.
- 733 Fu, C.C., Walia, V., Yang, T.F., Lee, L.C., Liu, T.K., Chen, C.H., Kumar, A., Lai,
734 T.H., & Wen, K.L. (2017a). Preseismic anomalies in soil-gas radon associated
735 with 2016 $M6.6$ Meinong earthquake, Southern Taiwan. *Terrestrial, Atmospheric*
736 *and Oceanic Sciences*, 28(5), 787-798.
- 737 Fu, C.C., Yang, T.F., Tsai, M.C., Lee, L.C., Liu, T.K., Walia, V., Chen, C.H., Chang,
738 W.Y., Kumar, A., & Lai, T.H. (2017b). Exploring the relationship between soil
739 degassing and seismic activity by continuous radon monitoring in the
740 Longitudinal Valley of eastern Taiwan. *Chemical Geology*, 469, 163-175.
- 741 Fu, C.C., Lee, L.C., Yang, T.F., Lin, C.H., Chen, C.H., Walia, V., Liu, T.K.,
742 Ouzounov, D., Giuliani, G., Lai, T.H., & Wang, P.K. (2019). Gamma ray and
743 radon anomalies in Northern Taiwan as a possible pre-earthquake indicator
744 around the plate boundary. *Geofluids*, 2019 Article ID 4734513, 14pp,
745 doi:10.1155/2019/4734513.
- 746 Genzano, N., Filizzola, C., Paciello, R., Pergola, N., & Tramutoli, V. (2015). Robust
747 Satellite Techniques (RST) for monitoring earthquake prone areas by satellite
748 TIR observations: the case of 1999 Chi-Chi earthquake (Taiwan). *Journal of*
749 *Asian Earth Sciences*, 114, 289-298, doi:10.1016/j.jseaes.2015.02.010.

- 750 Gorny, V.I., Salman, A.G., Tronin, A.A., & Shilin, B.B. (1988). The Earth outgoing
751 IR radiation as an indicator of seismic activity. *Proceedings of Academy of*
752 *Sciences, USSR*, 301, 67-69.
- 753 Hull, J. (1988). Thickness–displacement relationships for deformation zones. *Journal*
754 *of Structural Geology*, 10, 431-435. [http://dx.doi.org/10.1016/0191-](http://dx.doi.org/10.1016/0191-8141(88)90020-X)
755 8141(88)90020-X.
- 756 Irwin, G.R. (1958). Fracture. In: Flugge, S. (Ed.), *Handbook of Physics*, Springer-
757 Verlag Berlin pp6551-6590.
- 758 Kanamori, H., & Heaton, T.H. (2000). Microscopic and macroscopic physics of
759 earthquakes. In: Rundle, J.B., Turcotte, D.L., & Klein, W. (Eds.), *Geocomplexity*
760 *and the Physics of Earthquakes*, Vol. 120, AGU, Washington DC, USA
761 pp147-163, doi:10.1029/GM120p0147.
- 762 Kanamori, H., & Stewart, G.S. (1978). Seismological aspects of Guatemala
763 earthquake of February 4, 1976. *Journal of Geophysical Research*, 83, 3427-
764 3434.
- 765 Kano, M., Fukuda, J., Miyazaki, S., & Nakamura, M. (2018). Spatiotemporal
766 evolution of recurrent slow slip events along the Southern Ryukyu Subduction
767 Zone, Japan, from 2010 to 2013. *Journal of Geophysical Research Solid Earth*,
768 213, 7090-7107. <https://doi.org/10.1029/2018JB016072>.
- 769 Kim, K.H., Chiu, J.M., Pujol, J., Chen, K.C., Huang, B.S., Yeh, Y.H., & Shen, P.
770 (2005). Three-dimensional V_P and V_S structural models associated with the
771 active subduction and collision tectonics in the Taiwan region. *Geophysical*
772 *Journal International*, 162, 204-220.
- 773 Kuo, T., Chen, W., & Ho, C. (2018). Anomalous decrease in groundwater radon
774 before 2016 M_w 6.4 Meinong earthquake and its application in Taiwan. *Applied*
775 *Radiation Isotropy*, 136, 68-72.
- 776 Kuo, T., Chen, W., Ho, .C, Kuochen, H., & Chiang, C. (2019). In-situ radon
777 volatilization in an undrained fractured aquifer. *Proceedings of the 44th*
778 *Workshop Geothermal Reservoir Engineering*, Stanford Univ., Stanford,
779 California, USA, Feb. 11-13.
- 780 Kuo, T., Lin, C., Chang, G., Fan, K., Cheng, W., & Lewis, C. (2010). Estimation of
781 aseismic crustal strain using radon precursors of the 2003 M 6.8, 2006 M 6.1, and
782 2008 M 5.0 earthquakes in eastern Taiwan. *Natural Hazards*, 53, 219-228.
- 783 Lawn, B.R., & Wilshaw, T.R. (1975). *Fracture of Brittle Solids*. Cambridge Univ.

784 Press, Cambridge, UK.

785 Lee, C.R., & Cheng, W.T. (1986). Preliminary heat flow measurements in Taiwan,
786 presented in *the Fourth Circum-Pacific Energy and Mineral Resources*
787 *Conference*, Singapore.

788 Lin, C.H. (2000). Thermal modeling of continental subduction and exhumation
789 constrained by heat flow and seismicity in Taiwan. *Tectonophysics*, 324,
790 189-200.

791 Lin, C.H. (2016). Evidence for a magma reservoir beneath the Taipei metropolis of
792 Taiwan from both *S*-wave shadows and *P*-wave delays. *Scientific Report*, 6,
793 Article Number 39500.

794 Liu, K.K, Tsai, Y.B., Yeh, Y.H., Yui, T.F., & Teng, T.L. (1984). Variations of radon
795 content in ground waters and possible correlation with seismic activities in
796 northern Taiwan. *Pure Applied Geophysics*, 122, 231-244.

797 Ma, K.F., & Song, T.R.A. (2004). Thermo-mechanical structure beneath the young
798 orogenic belt of Taiwan. *Tectonophysics*, 388,
799 21-31, www.elsevier.com/locate/tecto.

800 Ma, K.F., Wang, J.H., & Zhao, D. (1996). Three-dimensional seismic velocity
801 structure of the crustal and uppermost mantle beneath Taiwan. *Journal of Physics*
802 *of the Earth*, 44, 85-105.

803 Main, I.G. (1988). Prediction of failure times in the earth for a time-varying stress.
804 *Geophysical Journal*, 92, 455-464.

805 Main, I.G., & Meredith, P.G. (1989). Classification of earthquake precursors from a
806 fracture mechanics model. *Tectonophysics*, 167, 273-283.

807 Marone, C. (1998). Laboratory-derived friction laws and their application to seismic
808 faulting. *Annual Review of Earth and Planetary Sciences*, 26, 643-696.

809 Marrett, R., & Allmendinger, R.W. (1990). Kinematic analysis of fault-slip data.
810 *Journal of Structural Geology*, 12, 973-986, [doi.org/10.1016/0191-](https://doi.org/10.1016/0191-8141(90)90093-E)
811 [8141\(90\)90093-E](https://doi.org/10.1016/0191-8141(90)90093-E).

812 Masci, F. (2010). On claimed ULF seismogenic fractal signatures in the geomagnetic
813 field. *Journal of Geophysical Research*, A10236. [http://dx.doi.org/10.1029/](http://dx.doi.org/10.1029/2010JA015311)
814 [2010JA015311](http://dx.doi.org/10.1029/2010JA015311).

815 Masci, F. (2011a). On the seismogenic increase of the ratio of the ULF geomagnetic
816 field components. *Physics of Earth and Planetary Interiors*, 187,
817 19-32. <http://dx.doi.org/10.1016/j.pepi.2011.05.001>.

- 818 Masci, F. (2011b). On the recent reaffirmation of ULF magnetic earthquakes
819 precursors. *Natural Hazards and Earth System Sciences*, 11, 2193-2198,
820 doi:10.5194/nhess-11- 2193-2011.
- 821 Masci, F. (2011c). On the ULF magnetic ratio increase before the 2008 Iwate–Miyagi
822 Nairiku earthquake by Hirano and Hattori (2011). *Journal of Asian Earth*
823 *Sciences*, 56, 258- 262.
- 824 Masci, F. (2012). The study of ionospheric anomalies in Japan area during 1998–2010
825 by Kon *et al.*: an inaccurate claim of earthquake-related signatures? *Journal of*
826 *Asian Earth Sciences*, 57, 1-5; doi:10.1016/j.jseaes.2012.06.009.
- 827 Masci, F., & Di Persio M. (2012). Retrospective investigation of geomagnetic field
828 time series during the 2009 L’Aquila seismic sequence. *Tectonophysics*. 530-531,
829 310-317. <http://dx.doi.org/10.1016/j.tecto.2012.01.008>.
- 830 Meredith, P.G., & Atkinson, B.K. (1983). Stress corrosion and acoustic emission
831 during tensile crack propagation in Whh Sill dolerite and other basic rocks.
832 *Geophysical Journal of the Royal astronomical Society*, 75, 1-21.
- 833 Molchanov, O.A., & Hayakawa, M. (1995). Generation of ULF electromagnetic
834 emission by microfracturing. *Geophysical Research Letters*, 22(22), 3091-3094.
- 835 Ouzounov, D., & Freund, F. (2004). Mid-infrared emission prior to strong
836 earthquakes analyzed by remote sensing data. *Advance of Space Research*, 33,
837 268-273, doi:10.1016/s0273-1177(03)00486-1.
- 838 Ouzounov, D., Pulinets, S. Kafatos, M., & Taylor, P. (2018). Thermal radiation
839 anomalies associated with major earthquakes. In: Ouzounov, D., Pulinets, S.,
840 Hattori, K., & Taylor, P. (Eds.), *Pre-Earthquake Processes: A Multidisciplinary*
841 *Approach to Earthquake Prediction Studies*, AGU Geophys. Monog. Series 234,
842 pp259-274, doi:10.1002/ 9781119156949.ch15.
- 843 Ouzounov., D., Bryant, N., Logan, T., Pulinets, S., & Taylor, P. (2006). Satellite
844 thermal IR phenomena associated with some of the major earthquakes in
845 1999–2003. *Physics and Chemistry of the Earth, Parts A/B/C*, 31(4-9), 154-163,
846 doi:10.1016/j.pce.2006.02.036.
- 847 Ouzounov., D., Liu, D., Kang, C.L., Cervone, G., Kafatos, M., & Taylor P. (2007).
848 Outgoing long wave radiation variability from IR satellite data prior to major
849 earthquakes. *Tectonophysics*, 431, 211-220, doi:10.1016/j.tecto.2006.05.042.
- 850 Ouzounov, D., Pulinets, S., Romanov, A., Romanov Jr., A., Tsybulya, K., Davydenko,
851 D., Kafatos, M., & Taylor, P. (2011). Atmosphere-ionosphere response to the M9

852 Tohoku Earthquake revealed by joined satellite and ground observations.
853 *Earthquake Sciences*, 24, 557-564.

854 Pulinet, S.A., & Dunajec, M.A. (2007). Specific variations of air temperature and
855 relative humidity around the time of Michoacan earthquake M8.1 September 19,
856 1985 as a possible indicator of interaction between tectonic plates.
857 *Tectonophysics*, 431, 221-230, doi:10.1016/j.tecto.2006.05.044

858 Pulinet, S.A., & Ouzounov, D. (2011). Lithosphere-Atmosphere-Ionosphere
859 Coupling (LAIC) model—An unified concept for earthquake precursors
860 validation. *Journal of Asian Earth Sciences*, 41, 371-382,
861 doi:10.1016/j.jseaes.2010.03.00.

862 Pulinet, S., Ouzounov, D., Karelin, A., & Davidenko, D. (2018). Lithosphere–
863 Atmosphere–Ionosphere–Magnetosphere coupling – A concept for pre-
864 earthquake signals generation. In: Ouzounov, D., Pulinet, S., Hattori, K., Taylor,
865 P. (Eds.), *Pre-Earthquake Processes: A Multidisciplinary Approach to*
866 *Earthquake Prediction Studies*, AGU Geophys. Monog. Series 234, pp79-98.

867 Pulinet, S.A., Ouzounov, D., Karelin, A.V., Boyarchuk, K.A., & Pokhmelnikh, L.A.
868 (2006). The physical nature of the thermal anomalies observed before strong
869 earthquake. *Physics and Chemistry of the Earth*, 31, 143-153,
870 doi:10.1016/j.pce.2006.02.042.

871 Qiang, Z.-j., Xu, X.-D., & Dian, C.-G. (1997). Thermal infrared anomaly—precursor
872 of impending earthquakes. *Pure and Applied Geophysics*, 149, 159-171.

873 Rau, R.J., & Wu, F.T. (1995). Tomographic imaging of lithospheric structures under
874 Taiwan. *Earth and Planetary Science Letters*, 133, 517-532,
875 doi:10.1016/0012-821X(95) 00076-O.

876 Rudnicki, J.W. (1988). Physical models of earthquake instability and precursory
877 processes. *Pure and Applied Geophysics*, 126(2-4), 531-554.

878 Scholten, J.C., Osvath, I., & Khanh Pham, M. (2013). Ra measurements through
879 gamma spectrometric counting of radon progenies: How significant is the loss of
880 radon?. *Marine Chemistry*, 156, 146-152, [http://dx.doi.org/10.1016/j.marchem.](http://dx.doi.org/10.1016/j.marchem.2013.03.001)
881 2013.03.001.

882 Scholz, C.H. (1990). *The Mechanics of Earthquakes and Faulting*. Cambridge Univ.
883 Press, Cambridge, UK, 439pp.

884 Shin, T.C. (1992). The calculation of local magnitude from the simulated Wood-
885 Anderson seismograms of the short-period seismograms in the Taiwan area.

886 *Terrestrial, Atmospheric and Oceanic Sciences*, 4(2), 155-170.

887 Sibson, R.H. (1977). Fault rocks and fault mechanisms. *Journal of the Geological*
888 *Society of London*, 133, 191-213.

889 Sibson, R.H. (1992). Implications of fault-valve behavior for rupture nucleation and
890 recurrence. *Tectonophysics*, 211, 283-293.

891 Surkov, V.V., Pokhotelov, O.A., Parrot, M., & Hayakawa, M. (2006). On the origin
892 of stable IR anomalies detected by satellites above seismo-active regions.
893 *Physics and Chemistry of the Earth*, 31, 164-171, doi:10.1016/j.pce.2006.02.020.

894 Thomas, J.N., Love, J.J. & Johnson M.J.S. (2009a). On the reported magnetic
895 precursor of the 1989 Loma Prieta earthquakes. *Physics of Earth and Planetary*
896 *Interiors*, 173, 207-215. <http://dx.doi.org/10.1016/j.pepi.2008.11.014>.

897 Thomas, J.N., Love, J.J., Johnson M.J.S., & Yumoto, K. (2009b). On the reported
898 magnetic precursor of the 1993 Guam earthquake. *Geophysical Research Letters*,
899 36, L16301. <http://dx.doi.org/10.1029/2009GL039020>.

900 Tramutoli, V., Di Bello, G., Pergola, N., & Piscitelli, S. (2001). Robust satellite
901 techniques for remote sensing of seismically active areas. *Annual Geofisica*, 44,
902 295- 312.

903 Tramutoli, V., Filizzola, C., Genzano, N., & Lisi, M. (2018). Robust satellite
904 techniques for detecting preseismic thermal anomalies. In: Ouzounov, D.,
905 Pulinets, S., Hattori, K., & Taylor, P. (Eds.), *Pre-Earthquake Processes: A*
906 *Multidisciplinary Approach to Earthquake Prediction Studies*, AGU Geophys.
907 Monog. Series 234, pp243-258.

908 Tramutoli, V., Cuomo, V., Filizzola, C., Pergola, N., & Pietrapertosa, C. (2005).
909 Assessing the potential of thermal infrared satellite surveys for monitoring
910 seismically active areas: the case of Kocaeli (Izmit) earthquake, August 17, 1999.
911 *Remote Sensing on Environments*, 96, 409-426, doi:10.1016/j.rse.2005.04.006.

912 Tramutoli, V., Aliano, C., Corrado, R., Filizzola, C., Genoano, N., Lisi, M., Martinell,
913 G., & Pergola, N. (2013). On the possible origin of thermal infrared radiation
914 (TIR) anomalies in earthquake-prone areas observed using robust satellite
915 techniques (RST). *Chemical Geology*, 339, 157-168, doi:10.1016/j.chemgeo.
916 2012.10.042.

917 Tronin, A., Hayakawa, M., & Molchanov, O. (2002). Thermal IR satellite data
918 application for earthquake research in Japan and China. *Journal of Geodynamics*,
919 33, 519-534,

- 920 Tsai, Y.B. (1986). Seismotectonics of Taiwan. *Tectonophysics*, 125, 17-37.
- 921 Tsai, Y.B., Teng, T.L., Chiu, J.M., & Liu, H.L. (1977). Tectonic implications of the
922 seismicity in the Taiwan region. *Memorial of the Geological Society of China*, 2,
923 13-41.
- 924 Turcotte, D.L., & Schubert, G. (1982). *GEODYNAMICS – Applications of Continuum*
925 *Physics to Geological Problems*. Wiley, 450pp.
- 926 Unsworth, M.J., & Bedrosian, P.A. (2004). On the geoelectric structure of major
927 strike-slip faults and shear zones. *Earth, Planets and Space*, 56, 1177-1184.
- 928 Ustaszewski, K., Wu, Y.M., Suppe, J., Huang, H.H., Chang, C.H., & Carena, S.
929 (2012). Crust-mantle boundaries in the Taiwan - Luzon arc-continent collision
930 system determined from local earthquake tomography and 1D models:
931 implications for the mode of subduction polarity reversal. *Tectonophysics*, 578,
932 31-49, doi:10.1016/j.tecto.2011.12.029.
- 933 Wakita, H., Nakamura, Y., & Sano, Y. (1986). Background fluctuation in
934 groundwater radon observation. *Journal of Physics of the Earth*, 34, S81-S89.
- 935 Wakita, H., Nakamura, Y., Notsu, K., Noguchi, M., & Asada, T. (1980). Radon
936 anomaly: a possible precursor of the 1978 Izu-Oshima-kinkai earthquake.
937 *Science*, 207, 882-883
- 938 Wang, J.H. (1988). *b* values of shallow earthquakes in Taiwan. *Bulletin of the*
939 *Seismological Society of America*, 78, 1243-1254.
- 940 Wang, J.H. (1998). Studies of earthquake seismology in Taiwan during the
941 1897–1996 period. *Journal of the Geological Society of China*, 41, 291-336.
- 942 Wang, J.H. (2006). Energy release and heat generation during the 1999 Chi-Chi,
943 Taiwan, earthquake. *Journal of Geophysical Research*, 111, B11312,
944 doi:10.1029/2005JB004018.
- 945 Wang, J.H. (2017). Frictional and viscous effects on the nucleation phase of an
946 earthquake nucleation. *Journal of Seismology*, 21(6), 1517-1539.
- 947 Wang, J.H. (2018). A study of earthquake recurrence based on a one-body
948 spring-slider model in the presence of thermal-pressurized slip-weakening
949 friction and viscosity. *Natural Hazards and Earth System Sciences*, 18,
950 1969-1983, <https://doi.org/10.5194/nhess-18-1-2018>.
- 951 Wang, J.H. (2021a). Piezoelectricity as a mechanism on generation of electro-
952 magnetic precursors before earthquakes. *Geophysical Journal International*, 224,
953 682-700.

954 Wang, J.H. (2021b). A review on precursors of the 1999 M_w 7.6 Chi-Chi, Taiwan,
955 earthquake. *Terrestrial, Atmospheric and Oceanic Sciences*, 32(3), 275-304,
956 doi:10.3319/TAO.2021.03.24.0.

957 Wang, J.H. (2021c). A compilation of precursor times of earthquakes in Taiwan.
958 *Terrestrial, Atmospheric and Oceanic Sciences*, 32(4), 411-441, doi:10.3319/
959 TAO.2021.07.12.01.

960 Wang, J.H., Chen, K.C., & Lee, T.Q. (1994). Depth distribution of shallow
961 earthquakes in Taiwan. *Journal of the Geological Society of China*, 37, 125-142.

962 Wang, J.H., Chen, K.C., Leu, P.L., & Chang, C.H. (2016). Precursor times of
963 abnormal b -values prior to earthquakes. *Journal of Seismology*, 20, 905-919.
964 DOI:10.1007/s10950-016-9567-7.

965 Wang, L., & Zhu, C., 1984. Anomalous variations in ground temperature before
966 Tangshan and Haiching earthquake. *Journal of Seismological Research*, 7,
967 649-656.

968 Wu, F.T. (1978). Recent tectonics of Taiwan. *Journal of Physics of the Earth*
969 (Supplement), 26, S265-S299.

970 Wu, S.K., Chi, W.C. Chi1, Hsu, S.M., Ke, C.C., & Wang, Y. (2013). Shallow crustal
971 thermal structures of Central Taiwan foothills region. *Terrestrial, Atmospheric*
972 *and Oceanic Sciences.*, 24(4), Part II, 695-707, doi: 10.3319/TAO.2013.03.13.
973 01(T).

974 Yang, T.F., Fu, C.C., Walia, V., Chen, C.H., Chyi, L.L., Liu, T.K., Song, S.R., Lee,
975 M., Lin, C.W., & Lin, C.C. (2006). Seismo-geochemical variations in SW
976 Taiwan: multi-parameter automatic gas monitoring results. *Pure and Applied*
977 *Geophysics*, 163(4), 693-709.

978 Yerkes, R.F., Levvine, P., & Wentworth, C.M. (1985). Abnormally high fluid
979 pressures in the region of the Coalinga earthquake—a preliminary report. *Open*
980 *File Report, United States Geological Surveys*, 85(44), 237-375.

981 Yu, S.B., Chen, H.Y., & Kuo, L.C. (1997). Velocity field of GPS stations in the
982 Taiwan area. *Tectonophysics*, 274, 41-59, doi:10.1016/S0040-1951(96)00297-1.

983 Zencher, F., Bonafede, M., Stefansson, R., 2006. Near-lithostatic pore pressure at
984 seismogenic depths: a thermoporoelastic model. *Geophysical Journal*
985 *International*, 166, 1318-1334.

Figures

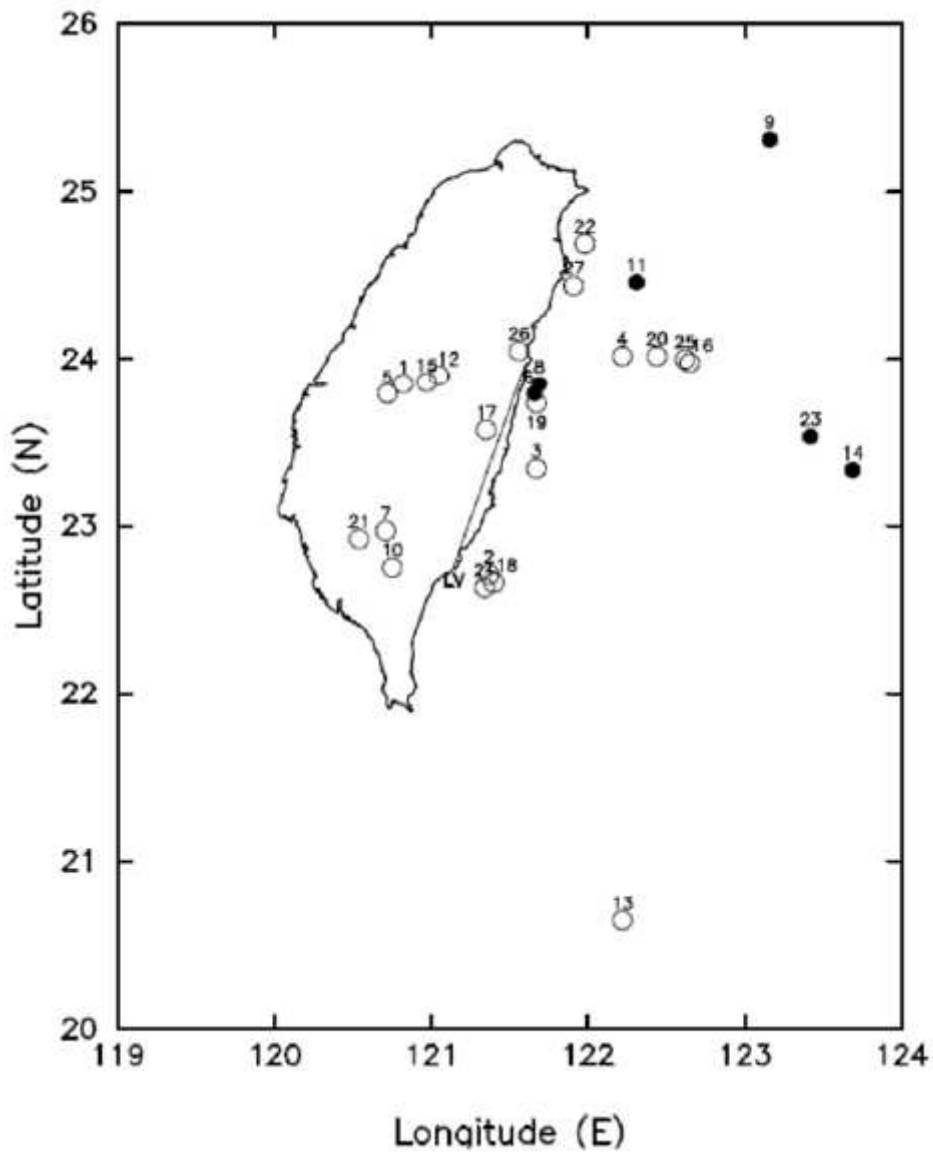


Figure 1

The figure shows the epicenters of 27 earthquakes listed in Table 1. EQ-01 event is the 1999 ML7.3 Chi-Chi earthquake. The open and solid circles denote the events with $d \leq 40$ km and those with $d > 40$ km, respectively. 'LV' represents the Longitudinal Valley.

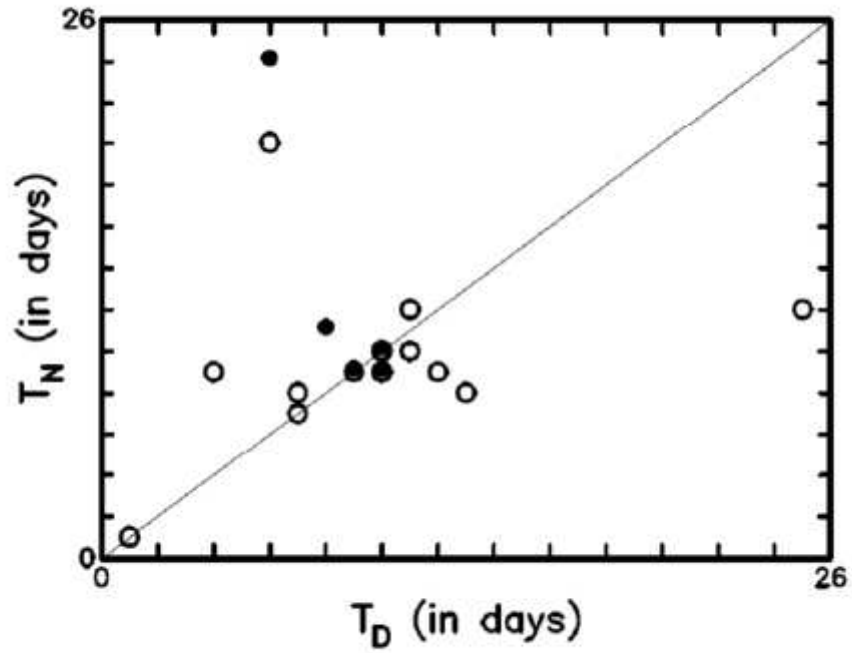


Figure 2

The plot of T_N versus T_D from Table 1. The thin solid line represents the bisecting line. Symbols: open circles for the events with $d \leq 40$ km and solid circles for those with $d > 40$ km.

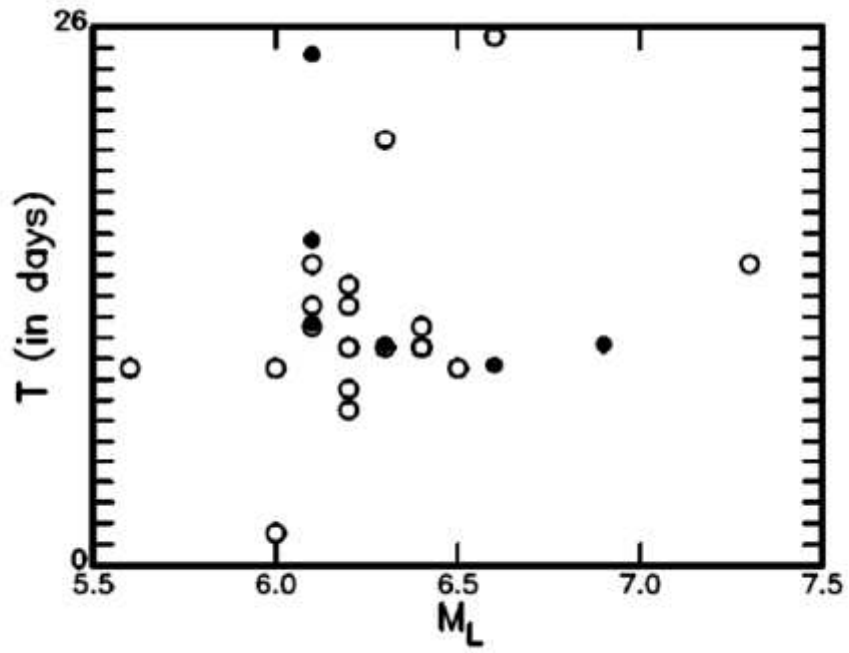


Figure 3

The plot of T versus M_L from Table 1. Symbols: open circles for the events with $d \leq 40$ km and solid circles for those with $d > 40$ km.

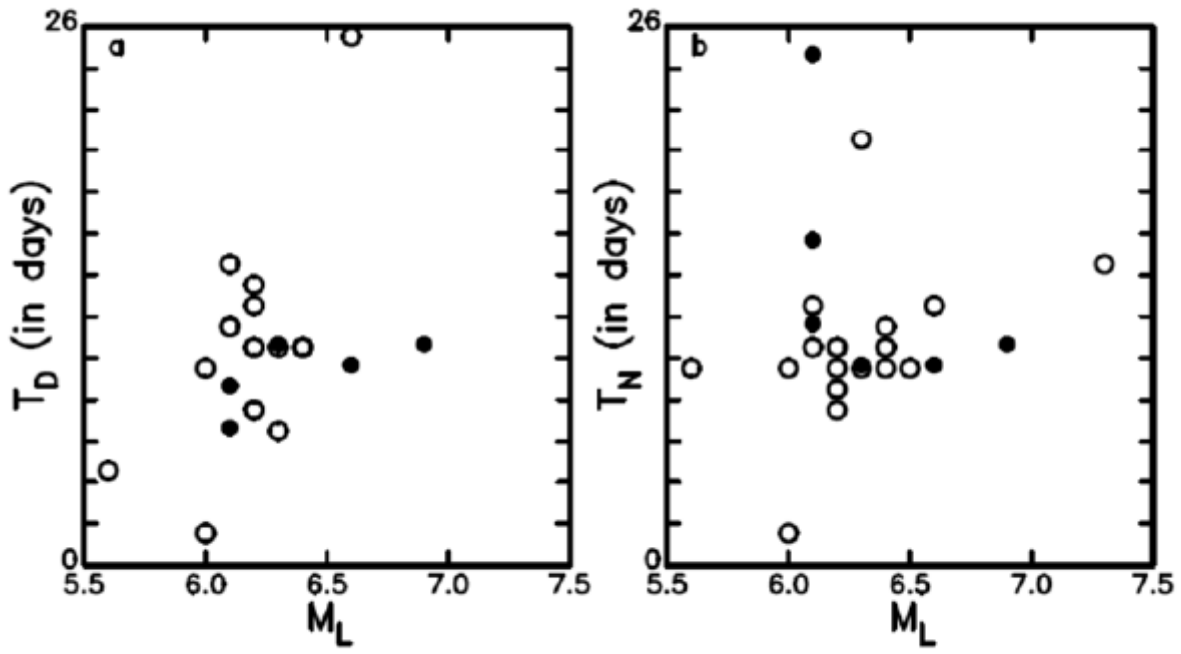


Figure 4

(a) for the plot of T_D versus M_L and (b) for the plot of T_N versus M_L from

Table 1. Symbols: open circles for the events with $d \leq 40$ km and solid circles for those with $d > 40$ km.

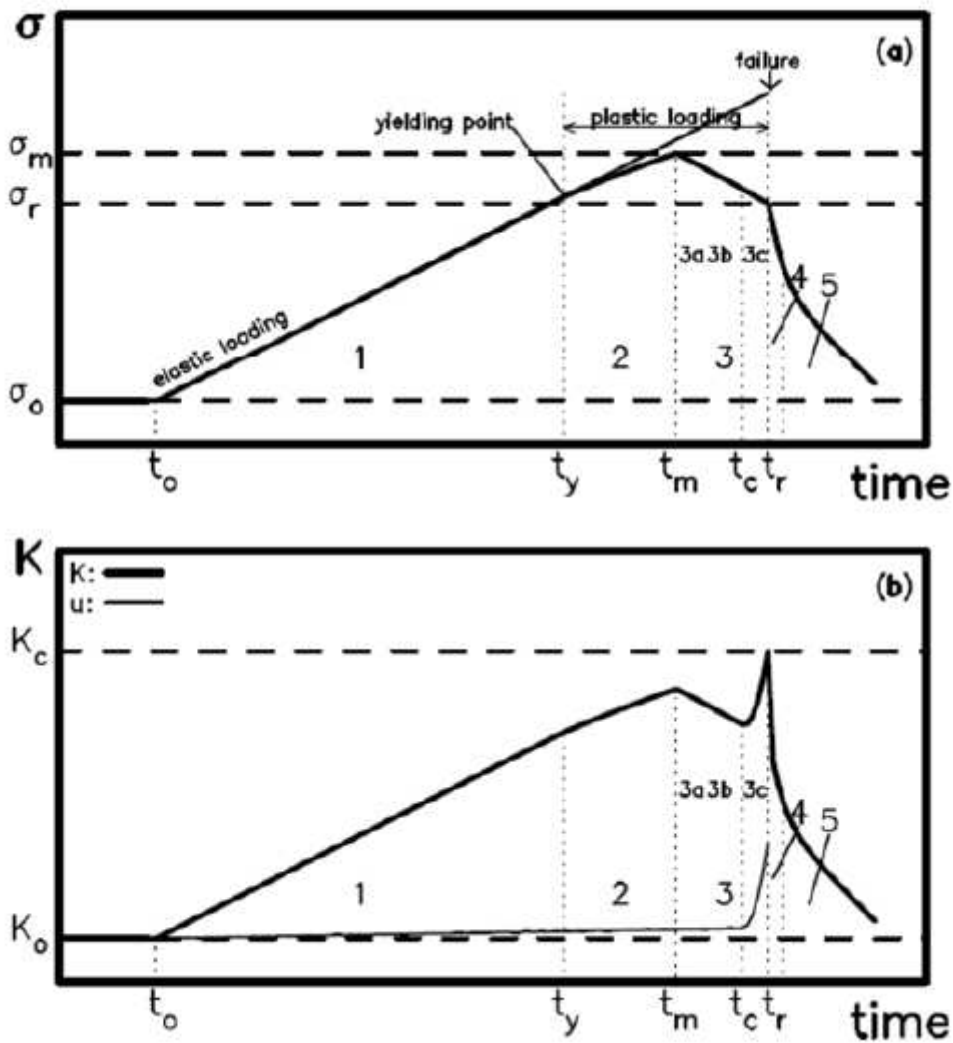


Figure 5

The temporal variations in stress, σ , stress intensity, K , and slip, u , in a fault zone: (a) for σ , and (b) for K (thick line) and u (thin line). The detailed description concerning this figure can see the text. (after Wang, 2021a)

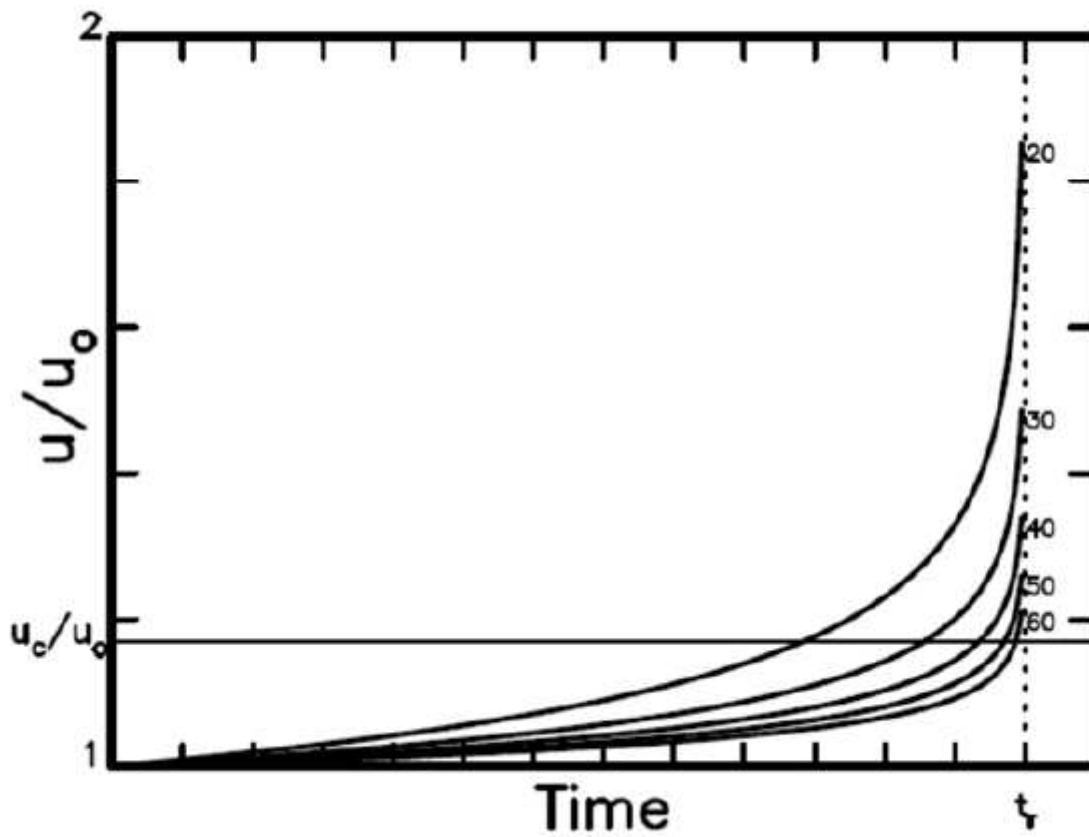


Figure 6

The plot shows the temporal variations in u/u_0 with time for five values of n , i.e., 20, 30, 40, 50, and 60. The thin horizontal line represents the ratio u_c/u_0 whose u_c is the critical value for producing a detectable surface temperature responsible for generation of TIR. (after Wang, 2021a)

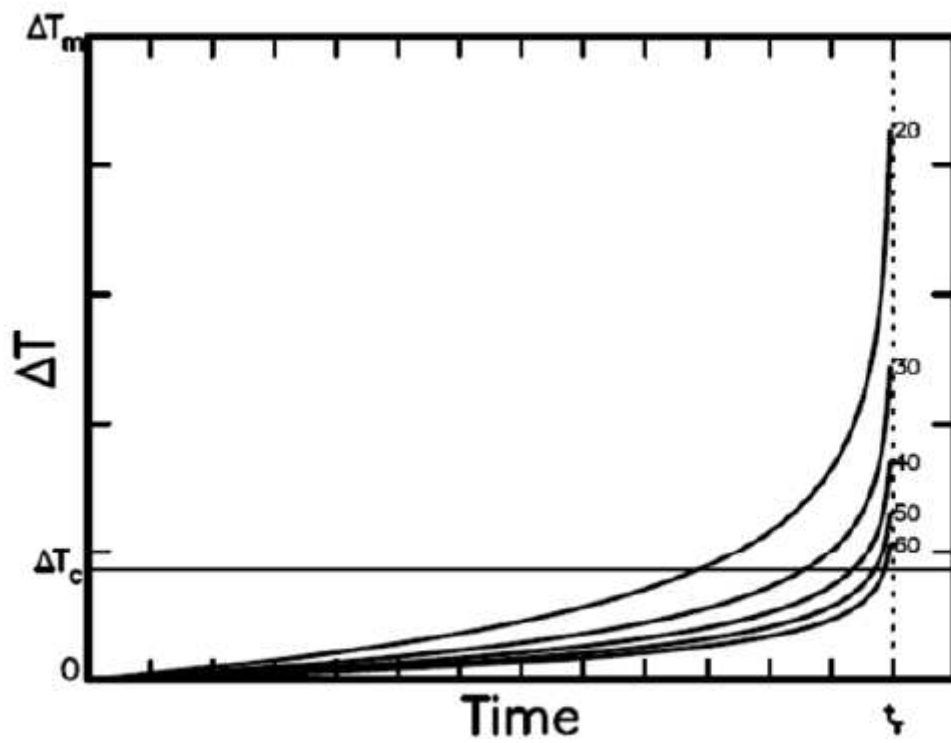


Figure 7

The plot shows the temporal variations in ΔT with time for five values of n , i.e., 20, 30, 40, 50, and 60. The thin horizontal line represents ΔT_c which is the critical value for producing the detectable TIR.

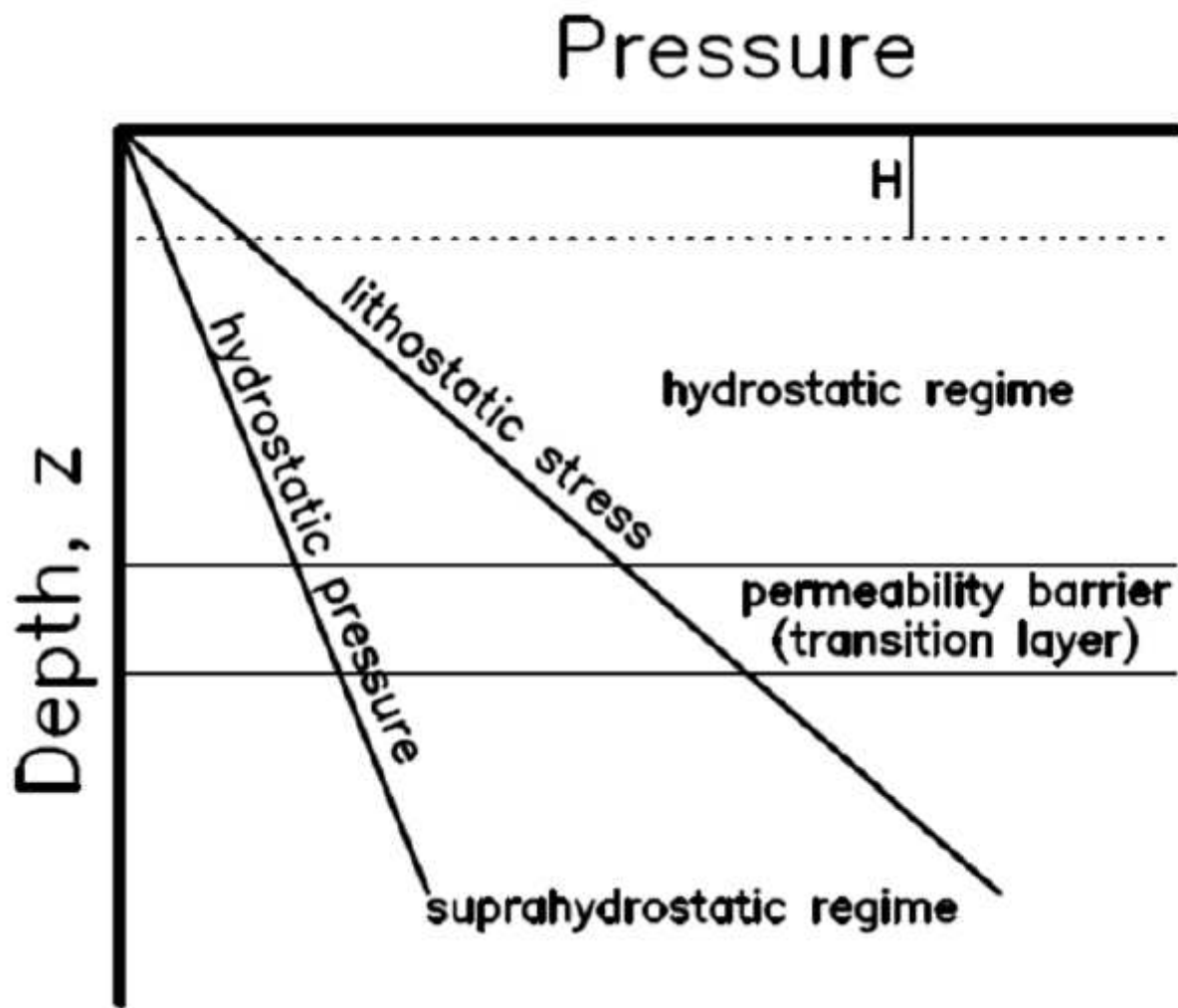


Figure 8

Schematic diagram for underground stress system: the hydrostatic regime, the permeability barrier (or transition layer) which is located in between two horizontal lines (~2 km for the upper line and ~6 km for the lower one), and the suprahydrostatic regime. The right inclined line represents the depth-increasing lithostatic stress, and the left line displays the depth-increasing hydrostatic pressure. The depth range in between the ground surface and a depth of H expresses the range within which the temperature rise produced by preseismic slip may be high enough for generating TIR anomalies as discussed in the text. The figure is modified from Wang (2021a).

Supplementary Files

This is a list of supplementary files associated with this preprint. Click to download.

- [TablesJeenHwaWang.pdf](#)